Journal of Computer Science

Original Research Paper

LT-LBP-Based Spatial Texture Feature Extraction with Deep Learning for X-Ray Images

Pankaja Lakshmi P. and Sivagami M.

School of Computer Science and Engineering, Vellore Institute of Technology, Chennai, India

Article history
Received: 06-10-2023
Revised: 17-11-2023
Accepted: 20-11-2023

Corresponding Author:
Pankaja Lakshmi P.
School of Computer Science and Engineering, Vellore Institute of Technology, Chennai, India
Email: pankajalakshmi.p@vit.ac.in

Abstract: The novel logarithmic transformation of Local Binary Pattern (LT-LBP) for texture feature extraction is used with Deep Learning (DL) models. The Computational complexity in the DL models asymptotically increases with the data sesssst and the depth of the layers in Convolutional Neural Networks (CNN). Pre-processing the images before training the DL model holds a strong impact on the operation speed and throughput. The proposed work encompasses LT-LBP for spatial texture feature extraction and is combined with the DL models. LT-LBP reduces the computation while extracting the texture information from the medical images. The computational cost for the model has been reduced in this study. The experiments were done with various DL models such as inception V3, Dense Net, Mobile Net, Efficient Net (B0-B7) VGG16, and RESNET50, and the results were analyzed. The features were extracted using LT-LBP and given as input to the DL models for classification. The retrospective study was done with 118 COVID-19 X-ray images collected from Chengalpattu Medical College Hospital, Chennai, and the remaining 8,224 images were taken from Kaggle. The combination of LT-LBP with RESNET50 shows better performance when compared to other models with an accuracy of 87%. The Area Under the Curve (AUC) for the proposed model is 88, 83 and 86% for COVID, non-COVID, and pneumonia classifications.

Keywords: LBP, LT-LBP, Texture Extraction, Machine Learning, Deep Learning

Introduction

Medical images are frequently used to identify and treat anomalies caused by various disorders of different body parts. Images are widely used to pinpoint numerous abnormalities and scans and X-rays are mainly used in diagnosing. Recent advances in imaging technology have made it possible for researchers to collect an extensive database of digital medical images. The electromagnetic spectrum includes radiation. Particle radiation contains positrons and neutrons, infrared, ultraviolet, X-rays, and gamma rays. 2000 shades of grey and contemporary CT scan machines may have as many as 4000 shades. It is beyond the power of human vision to differentiate between such a broad spectrum of gray-scale colors and the process of extracting textures from scanned images would have been essential for learning the model. Since the flow of diagnosis is a continuous procedure, addressing infections during X-ray and CT scanning for diagnosis is a time-consuming process.

The Local Binary Pattern (LBP) by Ojala *et al*. (1996) was used as an adequate feature extractor and was especially used for medical images. Since the images used are monochrome, LBP was chosen for texture identification because of its computational simplicity and high discriminative power and is a successful technique for producing high-level characteristics. Middle-level and low-level attributes were extracted to increase the classification accuracy and the feature's capacity for representation. Convolutional Neural Networks (CNN) operate on two-dimensional visual data, preserving the spatial relationships of the learned model. To reduce the computation logarithmic transformation of the Local Binary Pattern (LT-LBP) proposed by us, Lakshmi *et al*. (2021) extracted texture feature vectors from medical images. The development of highly discriminative and computationally effective local texture descriptors based on LBP has significantly improved the use of texture approaches in a wide range of challenges and applications in recent years Pietikäinen and Zhao (2015). In various disciplines, the method of LBP was widely applied to

image analysis and pattern recognition processes Kar and Banerjee (2021). The neonatal facial images for classifying various pain levels starting with the features of the face were used with LBP and its variants by Nanni *et al.* (2010). Modern diagnosis and the potential applications of edge extraction technologies require edge-based processing and analysis of medical images. Edge-aware filtering and improved Local Binary Patterns (EF-ALBP) were proposed by Qiao *et al*. (2022).

Mean distance LBP was proposed by Bedi and Sunkaria (2021). for texture retrieval from liver ultrasound images. The higher complexity and ambiguity of medical images were compared to ordinary image recognition. LBP was used for texture feature extraction from ultrasound and brain Magnetic Resonance Images (MRI) images by Zeebaree *et al.* (2019); Kaplan *et al*. (2020); Abbas *et al*. (2021). Images were processed and analyzed using various DL techniques, for image segmentation, image registration, and classification. To provide the predicted values and categorize the data, the pre-trained model is used in conjunction with data augmentation. In this study, we introduced a modified LBP algorithm that was applied to CT images to extract features and applied in ML classification algorithms such as Support Vector Machine (SVM) and Logistic Regression (LR). The gaps identified from the previous works are as follows.

The Computational cost is directly proportional to the depth of the layers and also in the preprocessing phase as the size of the dataset.

To address this, we tried a new method called LT-LBP for feature map generation and fed it to the DL model. The LT-LBP is the extended version of LBP. Since LBP has been used as the best image descriptor, feature extraction has been done by the transformed version of LBP with reduced computation.

The contributions in this study are:

- Inferring mathematical parameters from the distribution of pixels, the proposed methodology attempts to reduce the computing cost associated with the dataset by using LT-LBP (Lakshmi *et al*., 2021)
- The study has been extended with DL models to evaluate the performance
- The images have been divided into four quadrants and the texture feature has been extracted to avoid information loss

Related Work

A deep CNN was used to categorize the COVID X-rays by Abbas *et al*. (2021). Irregularities were handled by the class decomposition technique by Chen *et al.* (2021). The feature extraction used a Histogram of Oriented Gradients (HOG) and applied the CNN model for COVID-19 X-ray classification. Sweeping hyper-parameters through an experiment were replaced with the Bayesian optimization approach. The method increases recognition effectiveness by locating optimal network hyper-parameters and training options for CNN Loey *et al.* (2022). The attention mechanism with Efficient Net by Luz *et al*. (2021) yields better classification.

A modified version of the ResNet50 model has taken advantage of transfer learning and was given as a modified RESNET by Elpeltagy and Sallam (2021). The semi-supervised model could discriminate the target region from other anomalous locations using only a small amount of labeled data. In addition, the transfer learning technique is a practical choice for working with protected health information. Applying the previously trained models to previously undiscovered items is a zero-shot learning problem. Previous research on zero-shot learning for image classification has focused on medical image segmentation (Van Ginneken *et al*., 2001). Recent developments in deep learning have improved image classification and forecasting. Machine Learning (ML) and Deep Learning (DL) models possess both benefits and drawbacks. Table 1. shows a detailed survey of the DL models used in X-Ray classification.

Table 1: Related works based on COVID-19 X-ray/CT image classification with DL models

Author	Model	Dataset	Accuracy (%)
Ozturk *et al*. (2020)	Dark COVID Net	127 X-rays	98.8
Asif *et al*. (2020)	Coro Net	284-COVID, 310 -Normal, 330-Bacterial, 327 - Pneumonia	89.0 95.0
Born *et al*. (2020)	POCOVID -Net	654-COVID, 227-Bacterial, 172-Normal	89.0
Chen *et al*. (2021)	LUSS	31 (120,200)	87.0
Mahmud *et al*. (2020)	CovX Net	305-COVID, 1493-Non-COVID, 2780-Pneumonia, 1583-Normal	90.0
Qayyum *et al*. (2021)	Depth-wise CNN	435 X-Rays	87.4
Muhammad *et al*. (2022)	ResNet-50	5000 X-rays	89.0
Ardakani *et al*. (2020)	ResNet101, Inception	1020 CT images	99.5
Kulkarni *et al*. (2021)	DENSENE T121	663 X-rays	90.6

Materials and Methods

LBP uses local texture patterns to describe an image. By utilizing the patterns, it has been demonstrated that the present methods can improve the LBP as its variants. The main contribution of this study is towards LT-LBP with reduced computational cost. Research works are being continued to create appropriate frameworks for a variety of tasks, feature extraction, classification, and feature selection, along with the primary goal of enhancing the performance of automated systems for image annotation. Studies have adopted recent improvements in DL to interpret chest X-rays to boost efficiency and alleviate pressure on radiologists. X-ray imaging is a widely accepted medical procedure for examining abnormalities.

Pre-Processing

Infrared imaging systems suffer significantly from stripe noise effects in terms of image quality. Most of the frameworks like de-striping methods proposed in recent years. These techniques often fall into three categories: Prior-based, statistics-based, and deep techniques as described in (Yazdekhasty *et al*., 2021). Quantum noise has a negative impact on the images captured at low radiation doses. In some circumstances, such as fluoroscopy, the image intensifier picks up only a small portion of the signal, which causes a grainy appearance on the screen or in the pictures (Mistry *et al*., 2014). Owing to the pattern of the structure superimposed on random signal anomalies, fine images have a low contrast resolution of their details.

Noise Removal

Gaussian smoothing has been used to remove the noise from the images. In medical images, the sensor has noise due to temperature and illumination. Additionally, the electronic circuits connected to it add their own noise (Guan *et al*., 2019). Gaussian smoothing was used in this instance for noise removal to remove the noise from the X-ray images. A Gaussian filter was used with the Gaussian function as shown in Eq. 1. The noise removal is done by a 2D Gaussian filter and given in Eq. 1:

$$G(x,y) = \frac{1}{2\pi\sigma^2} e\left(\frac{x^2+y^2}{2\sigma^2}\right) \quad (1)$$

where, σ is the standard deviation. The average value of the surrounding or neighboring pixels was substituted for the noisy pixel in the image by Kumar and Nachamai (2017).

Feature Extraction Using LT-LBP

Texture refers to the surface of the specified feature in an image and it is certainly one of the key elements used in the identification of patterns and image processing. The eight elements form a Texture Unit (TU) and each of these elements can have one of three possible values (0, 1, or 2) that are drawn from neighboring pixels of 3×3. The total number of texture units that can describe spatial three-level patterns in a 3×3 neighboring pixel is 3^8 = 6561 by Wang and He (1990). The two-level derivation of the approach is used for describing LBP in a texture, it offers an effective method. Instead of 6561 potential texture units, there are only 2^8 = 256 in the two-level version (Ojala *et al*., 1996) Fig. 2 shows the neighboring pixel for the threshold used in LBP.

LBP was more effectively used as a local image descriptor than the other pre-processing texture extraction techniques. The LBP is transformed into LT-LBP by inferring the mathematical properties of basic logarithm and exponentiation in (Lakshmi *et al*., 2021). The binary number was converted into its equivalent decimal number. The conversion was performed using an exponential computation. The exponential computation was reduced to a linear computation using a logarithmic transformation. Figure 3 shows the LBP calculations for a single pixel in an image and Fig. 4 depicts the same calculation using LT-LBP for a single pixel.

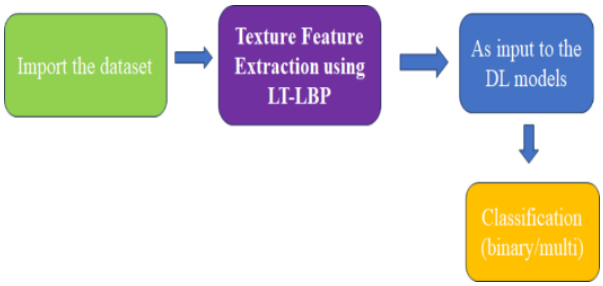

Fig. 1: Flow diagram of the model

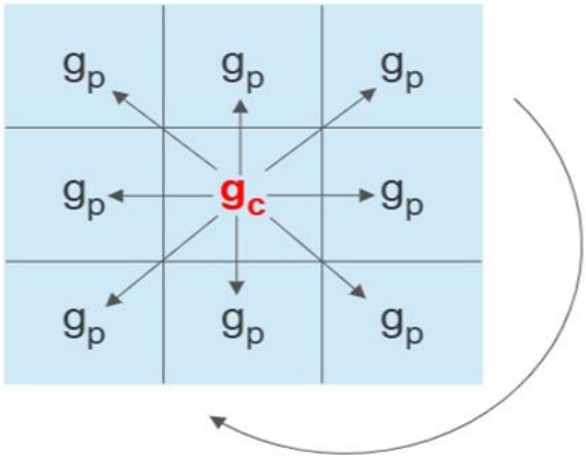

DOI: 10.3844/jcssp.2024.106.120

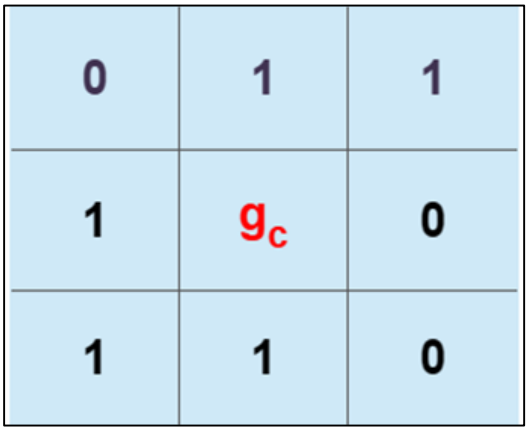

Fig. 2: Neighboring pixels from the image for LT-LBP

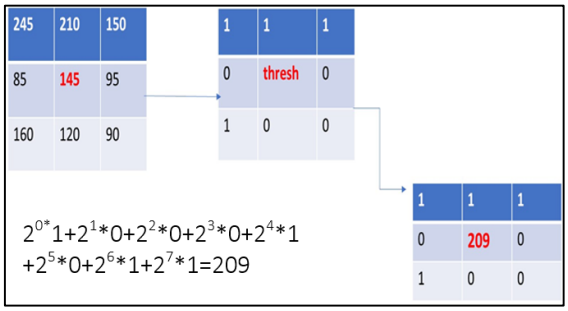

Fig. 3: LBP calculation for a single pixel in an image

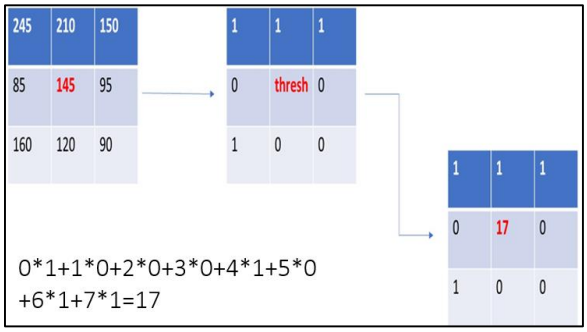

Fig. 4: LT-LBP calculation for a single pixel

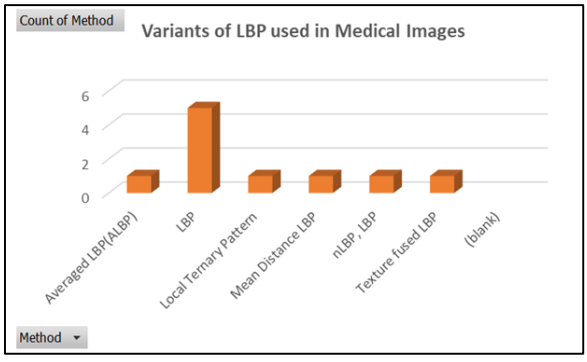

Fig. 5: The variants of LBP used in medical images

The center pixel value was considered as the threshold and the neighboring pixels were converted into binary values based on Eqs. 2-3. Based on local binary patterns and non-parametric differentiation of sample and prototype distributions, this technique efficiently classifies grey scale and rotation-invariant textures at many resolutions. The approach is based on the understanding that some LBPs known as "uniform" are essential components of local picture texture and their histogram of occurrence as very potent texture characteristics.

LBP is one of the best visual descriptors used in computer vision for image classification. Because of the invariance of LBP to scale and rotation, it has been employed as the finest visual descriptor in pre-processing. The center symmetric local derivative patterns of the combined first and second orders demonstrate a method called the Center Symmetric-Local Binary Pattern (CS-LBP) in Heikkila and Pietikainen (2006). The comparison of intensity space and illumination changes leads to less robust than edge responses. The Local Symmetric Directional Pattern (LSDP), a local feature descriptor for face recognition, effectively compresses facial textures into a small code by taking advantage of the gradient space structure of facial textures in Najmabadi and Moallem (2022). LBP was obtained using Eqs. 2-3:

$$LBP(g(x)) = \sum_{p=0}^{p-1} s(g_c - g_p)2^p \quad (2)$$

where, g_c represents the center pixel value and g_p denotes the neighboring pixel value, the function S is represented as:

$$s(x) = \begin{Bmatrix} 1 = if\ (x > 0) \\ 0 = otherwise \end{Bmatrix} \quad (3)$$

The calculation using LBP for a single pixel from an image is shown in Fig. 2.

Grey Level Co-occurrence Matrix (GLCM) and texture-based feature extraction are used as preprocessing for image classification. The pixel-based image processing technique used to estimate the value of its features is GLCM Garg and Dhiman (2021). However, the LBP descriptor is used in texture analysis of images in cases of illumination change because of its clarity in computation and resistance to such variations. The Illumination and ubiquitous nature in scales of length and rotation LBP (IRSLBP) descriptor achieved scale invariance by considering the circular neighbor set of each center pixel in addition to its regular neighbors. Additionally, the IRSLBP uses a local difference sign magnitude transform to separate the sign and magnitude components of the difference vector.

The pre-processing of MRI and CT images has an impact on the labels with the subsequent processing of these images. The enhancement in the CAD system requires improvement in the feature map generation.

It is essential to improve the image quality by eliminating the following from the brain MRI and CT images like skull segments; and skull and ribcage elements from the thorax and abdomen CT images (Pérez-García *et al*., 2021). Table 2 and Fig. 5 narrates the various methods of LBP used in medical image analysis recently.

The texture both natural and synthetic was quantitatively loaded with distributions of various local texture patterns that display abstract asymmetrical distributions.

The generation of rotation-invariant LBP variations is straightforward (Han *et al*. 2021; Zhao *et al*. 2011). The proposed model includes logarithmic functionalization of the conventional LBP technique from Eqs. (4-6) resulting in LT-LBP. According to the logarithmic and exponential rule, for every real number *b*, *x* and *n*:

$$x^n = b \equiv \log_x b = n \tag{4}$$

Table 2: LBP and its variants in medical image analysis

Author	Images	Method
Kaplan *et al*. (2020)	MRI-brain tumor	NLBP, LBP
Bedi and Sunkaria (2021)	Liver ultrasound	Mean distance LBP
Erfankhah *et al*. (2019)	Histopathology	LBP
Tuncer *et al*. (2020)	COVID X-ray	LBP
Chowdhary and Acharjya (2020)	Mammogram, CT, MRI	LBP
Garg and Dhiman (2021)	CORAL dataset	Texture fused LBP
Salih and Duffy (2022)	Dental image	Local ternary pattern
Hassaballah *et al*. (2019)	Ear images	Averaged LBP (ALBP)
Burrello *et al*. (2019)	Brain images (iEEG)	LBP
Pantazi *et al*. (2019)	Leaf images	LBP

Table 3: Proposed algorithm for LT-LBP

No:	Proposed Algorithm for LT-LBP in pre-processing images
Input:	Images after noise removal
output:	Feature vector from image textures using LT-LBP
1	let N be the number of images
2	let h, w be the height and width of the image
3	let g_c be the center pixel
4	let g_p be the neighboring pixels
5	for k in N
6	for i, j in height and width
7	for p in the range of neighboring pixels
8	If ($g_c - g_p > 0$)
9	$g_p = 1$
10	else
11	$g_p = 0$
12	$g_c = s(x) = \sum(g_c - g_p)*p$
13	Repeat step 6 for every pixel in the image
14	Repeat step 5 for every image

The *LBP* from Eq. 2 is transformed into *LT-LBP* by us in Eq. 5, by using the fundamental logarithmic characteristics from Eq. 4:

$$LT - LBP\big(g(x)\big) = \sum_{p=0}^{p-1} S\big(g_c - g_p\big)p \tag{5}$$

where, g_c represents the center pixel value and g_p denotes the neighboring pixel value and S is given by Eqs. 6:

$$s(x) = \begin{cases} 1 = if\ (x > 0) \\ 0 = otherwise \end{cases} \tag{6}$$

Equations 5-6 The result was calculated linearly as displayed to prevent the exponential computation and minimize the computational cost. The logarithmic properties were fulfilled and the textures were preserved. The exponential calculation was transformed into the linear computation. The LT-LBP calculation for a single pixel is shown in Fig. 4. By definition, exponents are logarithms and vice versa. Natural and binary logarithms carry similar properties. Figure 4 shows the LT-LBP method for feature map generation from Eqs. 5-6. The pseudocode for LT-LBP is shown in Table 3.

The LBP variants include the localized binary pattern created by holding the pixels relative to their median values throughout a 3×3 neighborhood. The Median Binary Pattern (MBP) technique was used for classifying textures with the center pixel included in the filtering process. Directional statistical data, in particular, the mean and standard deviation of the local absolute differences were obtained and enhanced the performance of Classification in LBP (Hafiane *et al*., 2008). Additionally, for more reliable directional statistical characteristics, the local difference is adaptively curtailed using least-squares estimation in Adaptive LBP (ALBP).

Deep Learning Models

The Convolution Neural Network (CNN) with feature map generation is shown in Fig. 6. The feature map is produced by the dot product of the kernel filter applied to the image in the convolution layer and the pixel intensity values of the images. Equation 10 refers to the convolution of the input image and the kernel filter:

$$o\{m,n\} = (I * k)[m,n] = \sum_i \sum_j I[m-i, n-j] * k[i,j] \tag{10}$$

where, k is the weight which is the kernel applied to the image I and m, n are the rows and columns of the result matrix generated and O is the output feature map. The convolution is followed by pooling and this layer is used to reduce the dimension of the feature map. The impact of noisy features is lessened by average pooling. However, because it gives equal weight to each component in the pooling region, background regions may predominate in the pool consequently, the power of discrimination may be diminished by representation (Nirthika *et al*., 2022).

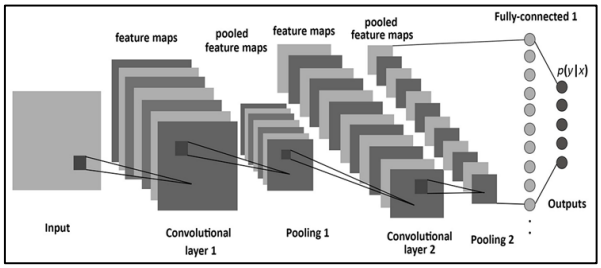

Fig. 6: Convolutional neural network for feature map generation Yu *et al.* (2018)

Average pooling may be more appropriate in the circumstances, like the separation of abnormalities from normal when the abnormality is widespread. The proposed method is implemented with average pooling and can be obtained from Eq. 11:

$$O_{avg}(x) = 1/N \sum_{i=1}^{N} |x_i| \quad (11)$$

The selection of average pooling was to prevent information loss from the X-ray images. Equation 11 represents the calculation of average pooling. Rank-based average pooling was used by Wang and He (1990). Eight-layer average pooling CNN was proposed by Kakarla *et al*. (2021) to address three class classifications for brain MRI. Max pooling is the commonly used pooling method in CNN and can be calculated using Eq. 12:

$$O_{max}(x) = \max(x_i)_{i=1}^{N} \quad (12)$$

The Rectified Linear Unit (ReLU) after the pooling layer in each convolution block is used as a non-linear activation function to reduce the generated output from Eq. 13:

$$ReLU = \begin{cases} 0 \; if \; (x < 0) \\ 1 \; if \; (x \geq 0) \end{cases} \quad (13)$$

A scaling function called Soft max converts numbers or logits into probabilities. Equation 14 provides the softmax function for multi-classification, which is used for the output layer:

$$Z(x_i) = \frac{e^{x_i}}{\sum e^{x_j}} \quad (14)$$

For binary classification, the sigmoid function is adopted and is given by Eq. 15:

$$Z(x_i) = \frac{1}{1+e^{-x_i}} \quad (15)$$

where, Z is the activation function for the output layer.

VGG16

A fine-tuned VGG16 model was used and worked with three sets of data, getting an accuracy of 79.8% for the binary classification of COVID and non-COVID. A deep CNN was introduced by Born *et al*. (2020) for COVID X-Ray classification and classification accuracy of 90.21% Simonyan and Zisserman (2014). Proposed a very deep convolutional neural network for massive images by the Visual Geometry Group (VGG).

Inception V3

The inception V3 model is used for feature extraction by Joshi *et al*. (2020). The inception V3 model comprises 43 layers and has a lower error rate. Gaur *et al*. (2021) investigated EfficientNetB0, VGG16, and inception V3 using Chest X-ray images. To identify pulmonary images and ultimately produce a workable and realistic computer-aided diagnostic model, the inception V3 was adopted by Wang *et al*. (2017). The dataset with 2437 training images, 660 test images and 200 validation images makes up the dataset. For the classification, deep learning architectures RESNET-101 and inception V3 have been used. When the results obtained are examined, the ResNet-101 architecture yields an accuracy rate of 84.09%, while the inception V3 architecture yields an accuracy rate of 87.42% by Demir *et al*. (2019).

Dense Net

Pertained weights are used for transfer learning as well, which helps the network to learn and perform better. The model used by Chauhan *et al*. (2021) was trained with 10 epochs. Modified Densenet201 was given by Hasan *et al*. (2021) using COVID-19 CT images. For the classification of pathological images, an Atrous Dense Net (ADN), a deep learning network, was proposed by Li *et al*. (2019) combining the atrous convolutions and dense blocks, the proposed ADN achieves multiscale feature extraction. The output of the Dense Layer receives the input features from all the previous layers. If *l* represents the layer and the output in Dense Net was obtained from Eq. 16:

$$O_l = H_l[O_0, O_1, O_2 \ldots \ldots O_{l-1}] \quad (16)$$

Mobile Net

Mobile NetV2 was used in the study of skin cancer image detection and classification on Android devices. In accordance with the results of the study, the best learning rate and epoch parameters were found to be 0.0001 for object detection and 15,000 epochs for classification Wibowo *et al*. (2020). Fine-tuned MobileNetV2 was proposed by Kaya and Gürsoy (2023) for COVID X-Ray classification.

Efficient Net

A nested network of pre-activated residual blocks, Atrous Spatial Pyramid Pooling (ASPP) blocks, and Attention Gates (AGs) make up Nested Efficient Net (NENet), which uses EfficientNetB4 as an encoder was developed by Siddique *et al*. (2022). EfficientNetB0 was fine-tuned and proposed for brain MRI classification by Shah *et al*. (2022).

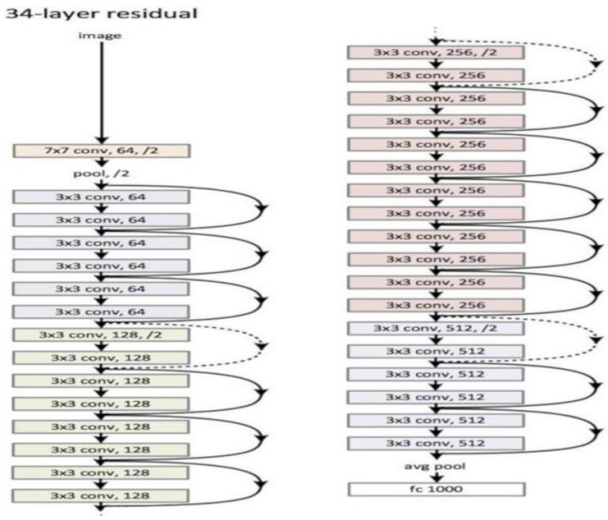

Fig. 7: Basic architecture of RESNET model (He *et al*., 2016)

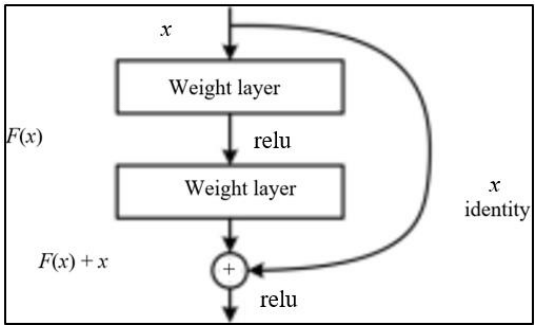

Fig. 8: Residual block (He *et al*., 2016)

RESNET50

He *et al*. (2016) proposed a deep residual network for image classification. RESNET50 with transfer learning technique was applied for breast cancer diagnosis using histopathological images by Al-Haija and Adebanjo (2020). Deep CNN can be trained more effectively with residual learning methods. From the input, a set of filters with trainable weights creates feature maps using the convolution operation. RESNET uses basic first-order algorithms for training and has shortcut connections across layers. RESNET skip connections mitigate the problem of vanishing gradients in deep neural networks by enabling the gradient to flow along an additional shortcut channel. These connections also aid by allowing the model to learn identity functions, ensuring that the higher layer performs at least as well as the lower layer. The RESNET50 architecture is shown in Fig. 7.

An increase in the number of layers increases the learning performance and accuracy. The output in each layer was combined with the residual function from Eq. 17 adopted from He *et al.* (2016):

$$O_k = O_k \sum_{i=k}^{K-1} F(x_i W_i) \quad (17)$$

where, K denotes the depth and k is any shallower unit.

The outputs from the previous layer were added to the outputs of stacked layers via the skip connections between layers shown in Fig. 8. The element-wise addition was conducted $F(x) + x$ after identity mapping of x.

On the CIFAR-10 dataset, the RESNET has tested the network with 100 and 1000 layers. The 152-layer ImageNet dataset has fewer parameters than the VGG16 network (Simonyan and Zisserman, 2014). is another well-liked Deep CNN architecture. At the ImageNet Large Scale Visual Recognition Challenge (ILSVRC) 2015 classification competition, an ensemble of deep residual networks placed first with a 3.57% error rate on the image net.

Impact of Deep Learning Models on Medical Images

The challenge of feature selection is resolved by deep learning algorithms, which can automatically extract essential characteristics from unprocessed input data. The development of artificial neural networks and comprehensive investigation of deep learning methodologies resulted in promising possible outcomes in medical imaging. Deep learning algorithms have the ability to help with early disease detection, which is essential for medical processes that involve the early identification, monitoring, diagnosis, and evaluation of different medical disorders. In medical imaging, deep learning algorithms have been applied to categorize, detect, and segment medical pictures based on various clinical applications, including digital histopathology images, X-ray images, computed tomography images, and mammography images. This research work focuses on the DL model which is specially used for medical image segmentation and classification. So the experiment was carried out by the trained DL models.

Experimental Analysis

Dataset

One of the most important tasks in image recognition and computer vision research is locating suitable datasets. The main drawback of the DL model in medical image analysis is that sufficient medical images for training sets were not available. The proposed model was evaluated with 8342 X-ray images and 118 X-ray images were collected from Chengalpattu Medical College Hospital, Chennai, India. These images were a part of the real-time training dataset and were used to validate the findings. The remaining 8224 chest X-ray images were taken from the COVID, non-COVID, and Pneumonia datasets from Kaggle. 848 COVID images, 4394 non-COVID X-ray images, and 3100 images of X-rays with Pneumonitis were included in the classification. There were 848

samples in total, 118 of them were real-time data. Here the class imbalance is one of the primary factors, which had an impact on training the dataset and accuracy metric. The raw image collection was organized and prepared for training the DL models. Data preparation and cleaning were essential parts of the DL process.

Experimental Setup

The experiment was done in an Asus Zen book with intel (R) core (TM) i7-10510U CPU @1.80 GHz. The implementation was done in the Python TensorFlow framework. A total of 8,342 images were given to the model for training and validation. Initially, the raw images collected were undergone with processing like data cleaning and resizing. Then the images are given for noise removal as shown in Fig. 1. As (Guan *et al*., 2019) said, the noise due to illumination and the circuit temperature would have been removed by Gaussian smoothing. Then the dataset was fed in texture feature map generation using LT-LBP. Texture extraction was adopted from (Wang *et al*., 2019; Ojala *et al*., 1996). This LBP was converted into LT-LBP by Lakshmi *et al*. (2021) from Eqs. (4-6). The feature map generated from LT-LBP is fed as input to the DL models such as inception V3, Dense Net, Mobile Net, Efficient Net (B0-B7), VGG16, and RESNET50. The proposed model was developed and examined with the DL models as mentioned. The hyperparameters with optimizers such as Adam and Stochastic Gradient Descent (SGD) have been applied. Adam optimizer from Eq. 18 with a learning rate of 0.001 gave better results:

$$m_n = E[A^n] \tag{18}$$

where, m is the moment of the certain variable, A is any variable and E is the expected value of the n variable.

Vani and Rao (2019) provided the analysis of various optimizers and the Adam optimizer resulted in better accuracy. The validation split ratio was taken as 80: 20. The batch size is 32. The batch size determines the number of samples to train the network. Data augmentation involves adding new data points from the given data, which was typically used to increase the number of training images. Based on the data augmentation approach, the images were split into four quadrants to increase the amount of data for training and validation. The metrics used for comparison are accuracy, precision, and recall. The inception V3, Dense Net, Mobile Net, Efficient Net (B0-B7), VGG16, and RESNET50 were used along with LT-LBP and the results are compared. For LT-LBP + RESNET50 the accuracy is 87%. The results are shown in Table 3. The experiment was continued with binary and multi-classification for analyzing the performance of LT-LBP for both binary (COVID/Non-COVID) and multi-classification with COVID, Non-COVID, and Pneumonia. RESNET50, with LT-LBP as feature map generation, results in better performance. Categorical cross entropy and Binary cross entropy are applied in the model for multi and binary classification. Normalization was done on the data before it was provided as input to the convolutional layer. Each model was experimented with 50 epochs. The accuracy is calculated by Eq. 19:

$$Accuracy = \frac{(TP + TN)}{(TP + TN + FP + FN)} \tag{19}$$

where, *TP* is True Positive and *TN* is True Negative, *FP* is False Positive and *FN* is False Negative. The precision was derived from Eq. 20 and measures how precisely the model identified a sample as positive:

$$Precision = \frac{TP}{(TP + FP)} \tag{20}$$

The recall was determined as the proportion of positive samples that were correctly identified as positive to all positive samples. The recall measures how well the model can identify positive samples. The more positive samples are identified, the larger the recall, and was calculated from Eq. 21. Table 4 and Fig. 9 show the accuracy, precision, and recall for the evaluated deep learning models such as Dense Net, Inception, Mobile Net, Efficient Net(B0-B6) and VGG16 with LT-LBP:

$$Recall = \frac{TP}{(TP + FN)} \tag{21}$$

For further analysis, the RESNET50 model was chosen and LT-LBP was used for the feature vector. LT-LBP was continued with the provided hyper-parameters, as it demonstrates the impact of the pre-processing method and showed that the accuracy of the proposed methodology has increased as given in Table 5.

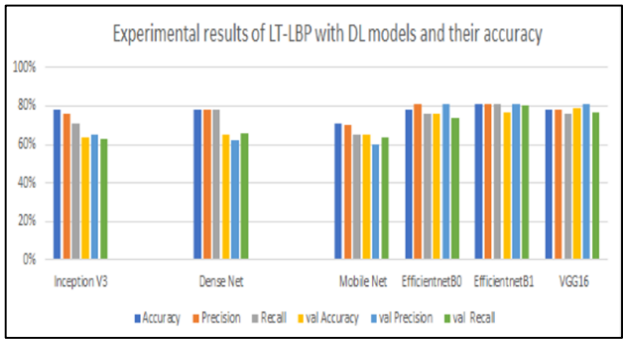

Fig. 9: Experimental results of DL models combined with LT-LBP

Table 4: Results from deep learning models with LT-LBP

Models	Accuracy (%)	precision (%)	Recall (%)	Val accuracy (%)	Val precision (%)	Val recall (%)
LT-LBP + Inception V3	78	76	71	64	65	63
LT-LBP + Dense Net	78	78	78	65	62	66
LT-LBP + Mobile Net	71	70	65	65	60	64
LT-LBP + Efficient netB0	78	81	76	76	81	74
LT-LBP + Efficient netB1	81	81	81	77	81	80
LT-LBP + VGG16	78	78	76	79	81	77

Table 5: Accuracy comparison for binary classification

Model	Class	Accuracy %
RESNET50	Binary	78
LT-LBP + RESNET50	Binary	87
LT-LBP + RESNET50	Binary (quadrants)	88

Results and Discussion

The experiment started with data cleaning and noise removal using a Gaussian filter and underwent LT-LBP processing implemented by us. Then the generated feature vector was fed into DL models and the results were analyzed. InceptionV3, Dense Net, Mobile Net, Efficient Net, VGG16, and RESNET50 were combined with LT-LBP and the accuracy has been compared.

Then the experiment was continued with four quadrants of the images. The model output is 87% for binary and 85% for multi-class, respectively as shown in Table 6.

The results are presented in Table 4. As from the literature survey 127 COVID X-Ray images got an accuracy of 87% with 1351 X-ray images achieving 89% of accuracy metrics. Also, Born *et al*. (2020); Mahmud *et al.* (2020); Qayyum *et al*. (2021); Muhammad *et al*. (2022) concluded with an accuracy of 89, 87, 90, and 90% respectively. But when compared to other models from the literature the dataset used in the previous work was trained with a limited number of training images. Johnson and Khoshgoftaar (2019) have discussed distinct methods to overcome the class imbalance in the data set.

Two-phase learning and dynamic sampling methods were suggested for DL models. Our model had been trained with more training images and also the real-time data were included for training as well as testing. A model has a small training error but a huge validation error, it is producing a high variance. Although the model doesn't display changes in training and validation errors, learning could be improved. A similar experiment was carried out at this point with the model being trained and the images divided into four quadrants. The accuracy has increased, yielding scores of 88-87%.

Figure 10 shows the performance of LT-LBP for feature extraction and combined with ML models. From the curve, it has been shown that the model is perfect and LT-LBP can be used in place of LBP. The LT-LBP was used in machine learning models including Support Vector Machine (SVM), Random Forest (RF), K-Nearest Neighbor (KNN), and Logistic Regression (LR) based on the prior research.

Since the feature generator, LT-LBP has shown better results from the prior work, the same is used for analyzing the DL models. Moreover, there was a modest increase in accuracy. In addition to unbalanced data, the complexity, and the overlap also affect the classification.

The model performance was compared with RESNET50 and LT-LBP + RESNET50 and is shown in Table 5. For binary and multi-classification, the accuracy variations rely on the number of images utilized in each class. Figure 13 shows the accuracy comparison of RESNET50 with LT-LBP + RESNET50 for binary classification.

The accuracy is the proportion of productive results obtained with the validation datasets, whereas the loss is the total errors based on the training and validation datasets. The images were divided into four quadrants and the feature map has been extracted using LT-LBP and fed into the DL models for evaluating the accuracy.

The Quadrant images produced an improvement in accuracy when the size of the image was reduced to half without changing the resolution of the image. The results are shown in Fig. 10. The results are less in train datasets but better in the validation datasets, the loss is decreased and accuracy is increased. Table 5 shows the results of the proposed model. The accuracy and loss curve for the experimented results are shown in Figs. 11,12 and 14. The Accuracy comparison of LT-LBP with ResNet50 is shown in Fig. 13.

Table 6: Accuracy comparison for Multi classification

Model	Class	Accuracy %
RESNET50	Multi	75
LT-LBP + RESNET50	Multi	85
LT-LBP + RESNET50	Multi (quadrants)	87

DOI: 10.3844/jcssp.2024.106.120

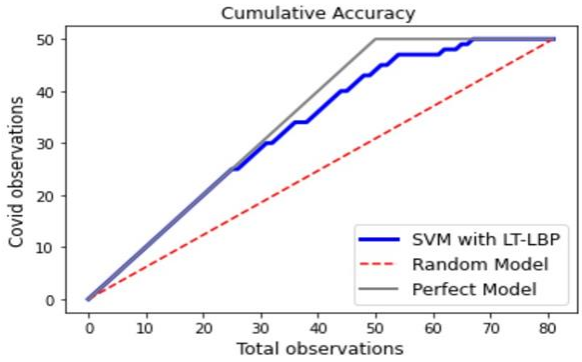

Fig. 10: Cumulative accuracy file (CAP) Lakshmi *et al*., 2021

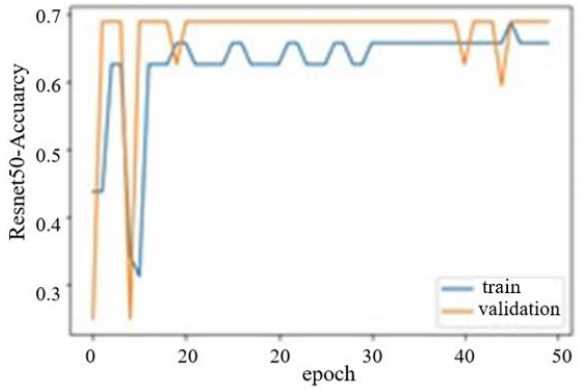

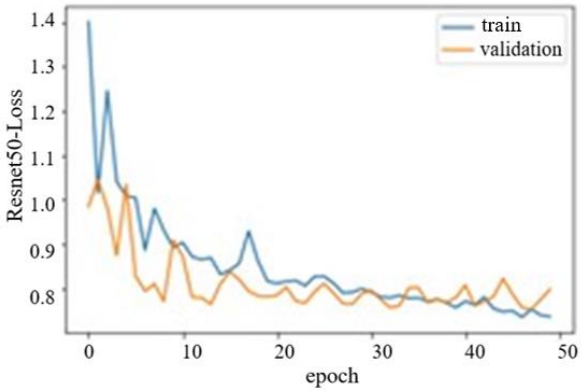

Fig. 11: Accuracy and loss curve for ResNet50

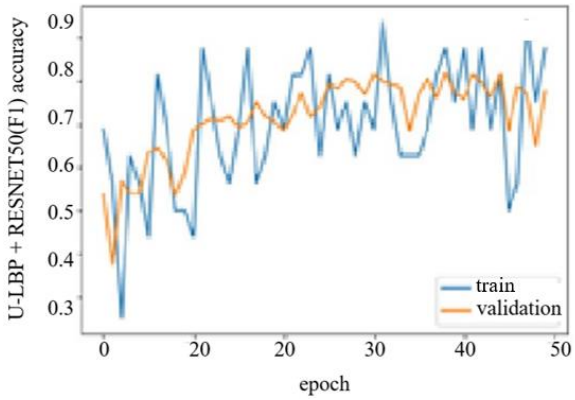

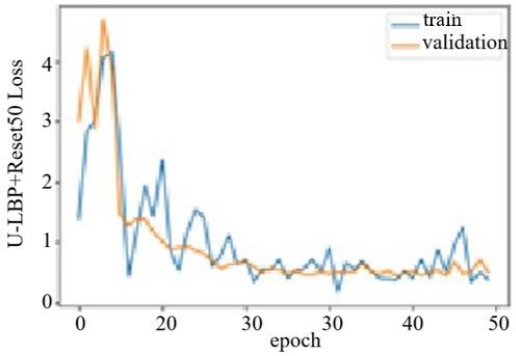

Fig. 12: Accuracy and loss curve for LT-LBP + ResNet 50

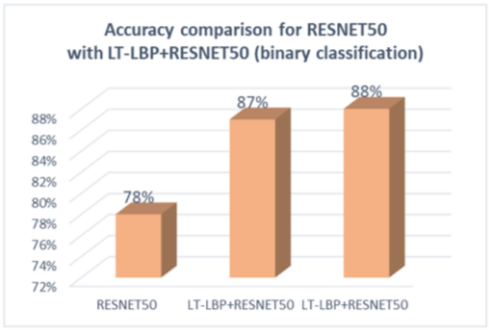

Fig. 13: Accuracy comparison for ResNet 50 with LT-LBP + ResNet 50 (binary classification)

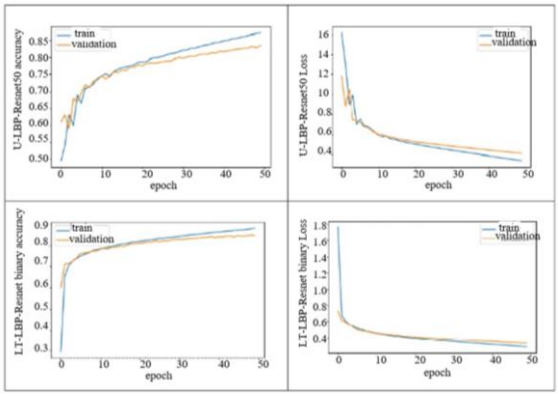

Fig. 14: Accuracy and loss curve for LT-LBP + ResNet50 for quadrant images

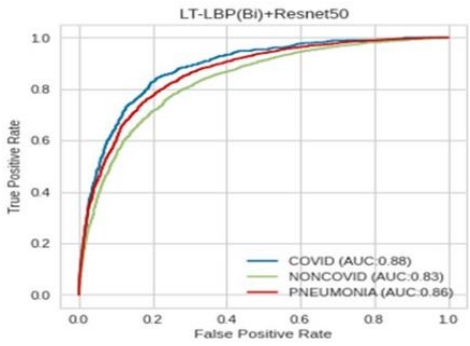

Fig. 15: Area under the curve for LT-LBP + ResNet50

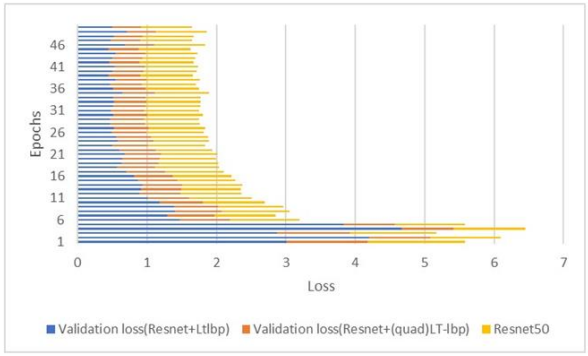

Fig. 16: Comparison of validation loss for ResNet50, LTLBP + ResNet50, LT-LBP (quadrants) + ResNet50

The AUC for the proposed model is 91%. The results are displayed in Fig. 15. The models VGG16 and RESNET50 yield the most significant outcomes. The experiment is then continued by extracting LT-LBP texture features. Tuncer *et al*. (2020) proposed Relief and this method was adopted for images which were then divided into four quadrants the quadrants are LT-LBP was used and the data was fed in RESNET50, which produces better accuracy.

The temporal complexity of an algorithm serves as an indicator of its speed for a given input size. The amount of space that an algorithm uses in relation to the size of the input is defined as the algorithm's space complexity. Auxiliary space and input space are both parts of space complexity. As same as the time complexity, it is described according to a specific input size. Model complexity is influenced by the model framework selection and was discussed by Hu *et al*. (2021). Model type such as feed-forward Neural Networks or CNN, activation function such as sigmoid or ReLU, and other factors are included in the model framework element. The complexity measure criteria for various model frameworks may differ.

An efficient model has an Area Under the Curve (AUC) close to 1, indicating that it has a high level of separability. An AUC close to 0, which indicates the worst measure of separability, indicates a poor model. It predicts both 1s and 0s as 1. Moreover, if the AUC is 0.5, the model has absolutely no capacity for class separation.

The AUC for the proposed model is shown in Fig. 15. The complexity of a model is also influenced by the data used to train it. Data dimensionality, data distribution, and information volume assessed by Kolmogorov complexity are important criteria. L1 regularized SVM and LDA model are two models that are used to create the hybrid model. The predictive model's training time is decreased by reducing the temporal complexity of the forecasting model by removing irrelevant features from the feature space in Afshin-Pour *et al*. (2014).

When the data are not equally distributed then the class imbalance arises and the accuracy of the learning network could show variations. The lack of data is also one of the reasons for class imbalance in medical diagnosis. Other than the imbalanced data, the complexity and overlapping also influence the data reparability between classes (Abd Elrahman and Abraham (2013). The validation loss for the experimented results has been analyzed in Fig. 16. The use of LT-LBP and RESNET50 in combination decreased the validation loss more than in the RESNET50 model.

Conclusion

The LT-LBP as a texture feature extractor from COVID X-Ray images were used with DL models and the results have been studied. With the addition of ML models from the previous research, the study has been done and the outcomes have been examined. Thse outcomes revealed a notable increase in accuracy. In spite of the learning from the deep neural network Additionally, the extraction of texture features requires less computation. Data cleaning and noise removal were applied to the dataset and then LT-LBP texture extraction was performed in order to create feature vectors. Inception V3, Dense Net, MobileNet, Efficient Net (B0-B7), VGG16 and RESNET50 were among the DL models that the features were then loaded for training. All of the models had a class imbalance and the performance metrics were mostly determined by the data set. The class imbalance in the dataset had a significant impact on the model's performance. With 118 real-time datasets and 8342 training images, the proposed approach in this research achieved an accuracy of 87%. When applying the deep learning model to the data, additional research would have focused on the class imbalance in the data. Storage needs have increased from gigabytes to petabytes as the number of digitized images has expanded exponentially.

The dataset of COVID X-ray images is used in this study to examine the effectiveness of LT-LBP-based texture feature extraction using a DL model. At the preprocessing stage, texture features are created with the least amount of computational complexity. The model's accuracy has been compared to other deep learning models' accuracy. The results were more accurately achieved when the LT-LBP and RESNET-50 were coupled. So LT-LBP can be used as a feature extractor instead of LBP. The outcomes demonstrated the accuracy improvement in both ML and DL models. Additionally, the cost of computing to extract texture features was decreased from exponential to linear. Further research will focus on fine-tuning the model.

Acknowledgment

We would like to express our gratitude to Chengalpattu Medical College Hospital, Chengalpattu, Chennai for their help in collecting the images.

Funding Information

The Authors have not received any financial support or funding to report.

Author's Contributions

Pankaja Lakshmi P.: Conceptualization, Methodology, Software. Data curation, Writing- Original draft preparation.

Sivagami M.: Investigation, Validation, Supervision.

Ethics

I undersigned that this article has not been published elsewhere. The authors declare no conflict of interest.

References

Abbas, A., Abdelsamea, M. M., & Gaber, M. M. (2021). Classification of COVID-19 in chest X-ray images using DeTraC deep convolutional neural network. *Applied Intelligence*, *51*, 854-864. https://doi.org/10.1007/s10489-020-01829-7

Abd Elrahman, S. M., & Abraham, A. (2013). A review of class imbalance problem. *Journal of Network and Innovative Computing*, *1*(2013), 332-340. https://ias04.softcomputing.net/jnic2.pdf

Afshin-Pour, B., Shams, S. M., & Strother, S. (2014). A hybrid LDA+ gCCA model for fMRI data classification and visualization. *IEEE Transactions on Medical Imaging*, *34*(5), 1031-1041. https://doi.org/10.1109/TMI.2014.2374074

Al-Haija, Q. A., & Adebanjo, A. (2020). Breast cancer diagnosis in histopathological images using resnet-50 convolutional neural network. *In 2020 IEEE International IOT, Electronics and Mechatronics Conference (IEMTRONICS)* 1-7. IEEE. https://doi.org/10.1109/IEMTRONICS51293.2020.9216455

Ardakani, A. A., Kanafi, A. R., Acharya, U. R., Khadem, N., & Mohammadi, A. (2020). Application of deep learning technique to manage COVID-19 in routine clinical practice using CT images: Results of 10 convolutional neural networks. *Computers in Biology and Medicine*, *121*, 103795. https://doi.org/10.1016/j.compbiomed.2020.103795

Asif, S., Wenhui, Y., Jin, H., & Jinhai, S. (2020). Classification of COVID-19 from chest X-ray images using deep convolutional neural network. *In 2020 IEEE 6th International Conference on Computer and Communications (ICCC)* 426-433. IEEE. https://doi.org/10.1109/ICCC51575.2020.9344870

Bedi, A. K., & Sunkaria, R. K. (2021). Mean distance local binary pattern: A novel technique for color and texture image retrieval for liver ultrasound images. *Multimedia Tools and Applications*, *80*, 20773-20802. https://doi.org/10.1007/s11042-021-10758-7

Born, J., Brändle, G., Cossio, M., Disdier, M., Goulet, J., Roulin, J., & Wiedemann, N. (2020). POCOVID-Net: Automatic detection of COVID-19 from a new lung ultrasound imaging dataset (POCUS). *arxiv Preprint arxiv:2004.12084*. https://doi.org/10.48550/arXiv.2004.12084

Burrello, A., Schindler, K., Benini, L., & Rahimi, A. (2019). Hyperdimensional computing with local binary patterns: One-shot learning of seizure onset and identification of ictogenic brain regions using short-time iEEG recordings. *IEEE Transactions on Biomedical Engineering*, *67*(2), 601-613. https://doi.org/10.1109/TBME.2019.2919137

Chauhan, T., Palivela, H., & Tiwari, S. (2021). Optimization and fine-tuning of dense net model for classification of COVID-19 cases in medical imaging. *International Journal of Information Management Data Insights*, *1*(2), 100020. https://doi.org/10.1016/j.jjimei.2021.100020

Chen, J., He, C., Yin, J., Li, J., Duan, X., Cao, Y., ... & Li, Q. (2021). Quantitative analysis and automated lung ultrasound scoring for evaluating COVID-19 pneumonia with neural networks. *IEEE Transactions on Ultrasonics, Ferroelectrics and Frequency Control*, *68*(7), 2507-2515. https://doi.org/10.1109/TUFFC.2021.3070696

Chowdhary, C. L., & Acharjya, D. P. (2020). Segmentation and feature extraction in medical imaging: A systematic review. *Procedia Computer Science*, *167*, 26-36. https://doi.org/10.1016/j.procs.2020.03.179

Demir, A., Yilmaz, F., & Kose, O. (2019). Early detection of skin cancer using deep learning architectures: Resnet-101 and inception-v3. *In 2019 Medical Technologies Congress (TIPTEKNO)* 1-4. IEEE. https://doi.org/10.1109/TIPTEKNO47231.2019.8972045

Elpeltagy, M., & Sallam, H. (2021). Automatic prediction of COVID-19 from chest images using modified ResNet50. *Multimedia Tools and Applications*, *80*(17), 26451-26463. https://doi.org/10.1007/s11042-021-10783-6

Erfankhah, H., Yazdi, M., Babaie, M., & Tizhoosh, H. R. (2019). Heterogeneity-aware local binary patterns for retrieval of histopathology images. *IEEE Access*, *7*, 18354-18367. https://doi.org/10.1109/ACCESS.2019.2897281

Garg, M., & Dhiman, G. (2021). A novel content-based image retrieval approach for classification using GLCM features and texture fused LBP variants. *Neural Computing and Applications*, *33*, 1311-1328. https://doi.org/10.1007/s00521-020-05017-z

Gaur, L., Bhatia, U., Jhanjhi, N. Z., Muhammad, G., & Masud, M. (2021). Medical image-based detection of COVID-19 using deep convolution neural networks. *Multimedia Systems*, 1-10. https://doi.org/10.1007/s00530-021-00794-6

Guan, J., Lai, R., & Xiong, A. (2019). Wavelet deep neural network for stripe noise removal. *IEEE Access*, *7*, 44544-44554. https://doi.org/10.1109/ACCESS.2019.2908720

Hafiane, A., Seetharaman, G., Palaniappan, K., & Zavidovique, B. (2008). Rotationally invariant hashing of median binary patterns for texture classification. *In Image Analysis and Recognition*: *5th International Conference, ICIAR 2008, Póvoa de Varzim, Portugal, Proceedings 5* 619-629. Springer berlin Heidelberg. https://doi.org/10.1007/978-3-540-69812-8_61

Han, Y., Song, T., Feng, J., & Xie, Y. (2021). Grayscale-inversion and rotation invariant image description with sorted LBP features. *Signal Processing: Image Communication*, *99*, 116491. https://doi.org/10.1016/j.image.2021.116491

Hasan, N., Bao, Y., Shawon, A., & Huang, Y. (2021). DenseNet convolutional neural networks application for predicting COVID-19 using CT image. *SN Computer Science*, *2*(5), 389. https://doi.org/10.1007/s42979-021-00782-7

Hassaballah, M., Alshazly, H. A., & Ali, A. A. (2019). Ear recognition using local binary patterns: A comparative experimental study. *Expert Systems with Applications*, *118*, 182-200. https://doi.org/10.1016/j.eswa.2018.10.007

He, K., Zhang, X., Ren, S., & Sun, J. (2016). Identity mappings in deep residual networks. In *Computer Vision-ECCV 2016: 14th European Conference, Amsterdam, The Netherlands, Proceedings, Part IV 14* 630-645. Springer International Publishing. https://doi.org/10.1007/978-3-319-46493-0_38

Heikkila, M., & Pietikainen, M. (2006). A texture-based method for modeling the background and detecting moving objects. *IEEE Transactions on Pattern Analysis and Machine Intelligence*, *28*(4), 657-662. https://doi.org/10.1109/TPAMI.2006.68

Hu, X., Chu, L., Pei, J., Liu, W., & Bian, J. (2021). Model complexity of deep learning: A survey. *Knowledge and Information Systems*, *63*, 2585-2619. https://doi.org/10.1007/s10115-021-01605-0

Johnson, J. M., & Khoshgoftaar, T. M. (2019). Survey on deep learning with class imbalance. *Journal of Big Data*, *6*(1), 1-54. https://doi.org/10.1186/s40537-019-0192-5

Joshi, K., Tripathi, V., Bose, C., & Bhardwaj, C. (2020). Robust sports image classification using inception V3 and neural networks. *Procedia Computer Science*, *167*, 2374-2381. https://doi.org/10.1016/j.procs.2020.03.290

Kakarla, J., Isunuri, B. V., Doppalapudi, K. S., & Bylapudi, K. S. R. (2021). Three-class classification of brain magnetic resonance images using average-pooling convolutional neural network. *International Journal of Imaging Systems and Technology*, *31*(3), 1731-1740. https://doi.org/10.1002/ima.22554

Kaplan, K., Kaya, Y., Kuncan, M., & Ertunç, H. M. (2020). Brain tumor classification using modified Local Binary Patterns (LBP) feature extraction methods. *Medical Hypotheses*, *139*, 109696. https://doi.org/10.1016/j.mehy.2020.109696

Kar, C., & Banerjee, S. (2021). Intensity prediction of tropical cyclone using multilayer multi-block local binary pattern and tree-based classifiers over North Indian Ocean. *Computers and Geosciences*, *154*, 104798. https://doi.org/10.1016/j.cageo.2021.104798

Kaya, Y., & Gürsoy, E. (2023). A mobilenet-based CNN model with a novel fine-tuning mechanism for COVID-19 infection detection. *Soft Computing*, *27*(9), 5521-5535. https://doi.org/10.1007/s00500-022-07798-y

Kulkarni, A. R., Athavale, A. M., Sahni, A., Sukhal, S., Saini, A., Itteera, M., ... & Kulkarni, H. (2021). Deep learning model to predict the need for mechanical ventilation using chest X-ray images in hospitalised patients with COVID-19. *BMJ Innovations*, *7*(2). https://doi.org/10.1136/bmjinnov-2020-000593

Kumar, N., & Nachamai, M. (2017). Noise removal and filtering techniques used in medical images. *Orient. J. Comput. Sci. Technol*, *10*(1), 103-113. https://doi.org/10.13005/ojcst/10.01.14

Lakshmi, P. P., Sivagami, M., & Balaji, V. (2021). A novel LT-LBP based prediction model for COVID-CT images with Machine Learning. *In 2021 International Conference on Information Systems and Advanced Technologies (ICISAT)* 1-5. IEEE. https://doi.org/10.1109/ICISAT54145.2021.9678196

Li, Y., Xie, X., Shen, L., & Liu, S. (2019). Reverse active learning based atrous densenet for pathological image classification. *BMC Bioinformatics*, *20*(1), 1-15. https://doi.org/10.1186/s12859-019-2979-y

Loey, M., El-Sappagh, S., & Mirjalili, S. (2022). Bayesian-based optimized deep learning model to detect COVID-19 patients using chest X-ray image data. *Computers in Biology and Medicine*, *142*, 105213. https://doi.org/10.1016/j.compbiomed.2022.105213

Luz, E., Silva, P., Silva, R., Silva, L., Guimarães, J., Miozzo, G., ... & Menotti, D. (2021). Towards an effective and efficient deep learning model for COVID-19 patterns detection in X-ray images. *Research on Biomedical Engineering*, 1-14. https://doi.org/10.1007/s42600-021-00151-6

Mahmud, T., Rahman, M. A., & Fattah, S. A. (2020). CovXNet: A multi-dilation convolutional neural network for automatic COVID-19 and other pneumonia detection from chest X-ray images with transferable multi-receptive feature optimization. *Computers in Biology and Medicine*, *122*, 103869. https://doi.org/10.1016/j.compbiomed.2020.103869

Mistry, A. R., Uzbelger Feldman, D., Yang, J., & Ryterski, E. (2014). Low dose x-ray sources and high quantum efficiency sensors: The next challenge in dental digital imaging? *Radiology Research and Practice*. https://doi.org/10.1155/2014/543524

Muhammad, L. J., Algehyne, E. A., Usman, S. S., Mohammed, I. A., Abdulkadir, A., Jibrin, M. B., & Malgwi, Y. M. (2022). Deep learning models for predicting COVID-19 using chest x-ray images. *Trends and Advancements of Image Processing and Its Applications*, 127-144. https://doi.org/10.1007/978-3-030-75945-2_6

Najmabadi, M., & Moallem, P. (2022). Local symmetric directional pattern: A novel descriptor for extracting compact and distinctive features in face recognition. *Optik*, *251*, 168331. https://doi.org/10.1016/j.ijleo.2021.168331

Nanni, L., Lumini, A., & Brahnam, S. (2010). Local binary patterns variants as texture descriptors for medical image analysis. *Artificial Intelligence in Medicine*, *49*(2), 117-125. https://doi.org/10.1016/j.artmed.2010.02.006

Nirthika, R., Manivannan, S., Ramanan, A., & Wang, R. (2022). Pooling in convolutional neural networks for medical image analysis: A survey and an empirical study. *Neural Computing and Applications*, *34*(7), 5321-5347. https://doi.org/10.1007/s00521-022-06953-8

Ojala, T., Pietikäinen, M., & Harwood, D. (1996). A comparative study of texture measures with classification based on featured distributions. *Pattern Recognition*, *29*(1), 51-59. https://doi.org/10.1016/0031-3203(95)00067-4

Ozturk, T., Talo, M., Yildirim, E. A., Baloglu, U. B., Yildirim, O., & Acharya, U. R. (2020). Automated detection of COVID-19 cases using deep neural networks with X-ray images. *Computers in Biology and Medicine*, *121*, 103792. https://doi.org/10.1016/j.compbiomed.2020.103792

Pantazi, X. E., Moshou, D., & Tamouridou, A. A. (2019). Automated leaf disease detection in different crop species through image features analysis and One Class Classifiers. *Computers and Electronics in Agriculture*, *156*, 96-104. https://doi.org/10.1016/j.compag.2018.11.005

Pérez-García, F., Sparks, R., & Ourselin, S. (2021). TorchIO: A Python library for efficient loading, preprocessing, augmentation and patch-based sampling of medical images in deep learning. *Computer Methods and Programs in Biomedicine*, *208*, 106236. https://doi.org/10.1016/j.cmpb.2021.106236

Pietikäinen, M., & Zhao, G. (2015). Two decades of local binary patterns: A survey. *In Advances in Independent Component Analysis and Learning Machines* 175-210. Academic Press. https://doi.org/10.1016/B978-0-12-802806-3.00009-9

Qayyum, A., Razzak, I., Tanveer, M., & Kumar, A. (2021). Depth-wise dense neural network for automatic COVID19 infection detection and diagnosis. *Annals of Operations Research*, 1-21. https://doi.org/10.1007/s10479-021-04154-5

Qiao, S., Yu, Q., Zhao, Z., Song, L., Tao, H., Zhang, T., & Zhao, C. (2022). Edge extraction method for medical images based on improved local binary pattern combined with edge-aware filtering. *Biomedical Signal Processing and Control*, *74*, 103-490. https://doi.org/10.1016/j.bspc.2022.103490

Salih, O., & Duffy, K. J. (2022). The local ternary pattern encoder-decoder neural network for dental image segmentation. *IET Image Processing*, *16*(6), 1520-1530. https://doi.org/10.1049/ipr2.12416

Shah, H. A., Saeed, F., Yun, S., Park, J. H., Paul, A., & Kang, J. M. (2022). A robust approach for brain tumor detection in magnetic resonance images using finetuned efficientnet. *IEEE Access*, *10*, 65426-65438. https://doi.org/10.1109/ACCESS.2022.3184113

Siddique, N., Paheding, S., Reyes Angulo, A. A., Alom, M. Z., & Devabhaktuni, V. K. (2022). Fractal, recurrent and dense U-Net architectures with efficientnet encoder for medical image segmentation. *Journal of Medical Imaging*, *9*(6), 064004-064004. https://doi.org/10.1117/1.JMI.9.6.064004

Simonyan, K., & Zisserman, A. (2014). Very deep convolutional networks for large-scale image recognition. *Arxiv Preprint Arxiv:*1409.1556. https://doi.org/10.48550/arXiv.1409.1556

Tuncer, T., Dogan, S., & Ozyurt, F. (2020). An automated residual exemplar local binary pattern and iterative relieff based COVID-19 detection method using chest X-ray image. *Chemometrics and Intelligent Laboratory Systems*, *203*, 104054. https://doi.org/10.1016/j.chemolab.2020.104054

Van Ginneken, B., Romeny, B. T. H., & Viergever, M. A. (2001). Computer-aided diagnosis in chest radiography: A survey. *IEEE Transactions on Medical Imaging*, *20*(12), 1228-1241. https://doi.org/10.1109/42.974918

Vani, S., & Rao, T. M. (2019). An experimental approach towards the performance assessment of various optimizers on convolutional neural network. *In 2019 3rd International Conference on Trends in Electronics and Informatics (ICOEI)* 331-336. IEEE. https://doi.org/10.1109/ICOEI.2019.8862686

Wang, C., Chen, D., Hao, L., Liu, X., Zeng, Y., Chen, J., & Zhang, G. (2019). Pulmonary image classification based on inception-v3 transfer learning model. *IEEE Access*, *7*, 146533-146541. https://doi.org/10.1109/ACCESS.2019.2946000

Wang, L., & He, D. C. (1990). Texture classification using texture spectrum. *Pattern Recognition*, *23*(8), 905-910. https://doi.org/10.1016/00313203(90)90135-8

Wang, S., Jiang, Y., Hou, X., Cheng, H., & Du, S. (2017). Cerebral micro-bleed detection based on the convolution neural network with rank based average pooling. *IEEE Access*, *5*, 16576-16583. https://doi.org/10.1109/ACCESS.2017.2736558

Wibowo, A., Hartanto, C. A., & Wirawan, P. W. (2020). Android skin cancer detection and classification based on mobilenetv2 model. *International Journal of Advances in Intelligent Informatics*, *6*(2), 135-148. https://doi.org/10.26555/ijain.v6i2.492

Yazdekhasty, P., Zindari, A., Nabizadeh-ShahreBabak, Z., Roshandel, R., Khadivi, P., Karimi, N., & Samavi, S. (2021). Bifurcated auto encoder for segmentation of COVID-19 infected regions in CT images. *In Pattern Recognition. ICPR International Workshops and Challenges: Virtual Event, Proceedings, Part II* 597-607. Springer International Publishing. https://doi.org/10.1007/978-3-030-68790-8_46

Yu, A. (2018). How to teach a computer to see with convolutional neural networks? Towards data science, *Towards Data Science*, *26*.

Zeebaree, D. Q., Haron, H., Abdulazeez, A. M., & Zebari, D. A. (2019). Trainable model based on new uniform LBP feature to identify the risk of the breast cancer. *In 2019 International Conference on Advanced Science and Engineering (ICOASE)* 106-111. IEEE. https://doi.org/10.1109/ICOASE.2019.8723827

Zhao, G., Ahonen, T., Matas, J., & Pietikainen, M. (2011). Rotation-invariant image and video description with local binary pattern features. *IEEE Transactions on Image Processing*, *21*(4), 1465-1477. https://doi.org/10.1109/TIP.2011.2175739